

Study of mineral dust entrainment in the planetary boundary layer by lidar depolarisation technique

By JUAN ANTONIO BRAVO-ARANDA^{1,2*}, GLORIA TITOS^{1,2},
MARÍA JOSÉ GRANADOS-MUÑOZ^{1,2}, JUAN LUÍS GUERRERO-RASCADO^{1,2},
FRANCISCO NAVAS-GUZMÁN^{1,2,3}, ANTONIO VALENZUELA^{1,2},
HASSAN LYAMANI^{1,2}, FRANCISCO JOSÉ OLMO^{1,2},
JAVIER ANDREY^{4†} and LUCAS ALADOS-ARBOLEDAS^{1,2},

¹Andalusian Institute for Earth System Research (IISTA-CEAMA), Granada, Spain; ²Department of Applied Physics, University of Granada, Granada, Spain; ³Institute of Applied Physics (IAP), University of Bern, Bern, Switzerland; ⁴Instituto Nacional de Técnica Aeroespacial (INTA), Torrejón de Ardoz, Spain

(Manuscript received 1 October 2014; in final form 7 April 2015)

ABSTRACT

Measurements on 27 June 2011 were performed over the Southern Iberian Peninsula at Granada EARLINET station, using active and passive remote sensing and airborne and surface in-situ data in order to study the entrainment processes between aerosols in the free troposphere and those in the planetary boundary layer (PBL). To this aim the temporal evolution of the lidar depolarisation, backscatter-related Angström exponent and potential temperature profiles were used in combination with the PBL contribution to the aerosol optical depth (AOD). Our results show that the mineral dust entrainment in the PBL was caused by the convective processes which 'trapped' the lofted mineral dust layer, distributing the mineral dust particles within the PBL. The temporal evolution of ground-based in-situ data evidenced the impact of this process at surface level. Finally, the amount of mineral dust in the atmospheric column available to be dispersed into the PBL was estimated by means of POLIPHON (Polarizing Lidar Photometer Networking). The dust mass concentration derived from POLIPHON was compared with the coarse-mode mass concentration retrieved with airborne in-situ measurements. Comparison shows differences below $50 \mu\text{g}/\text{m}^3$ (30% relative difference) indicating a relative good agreement between both techniques.

Keywords: Saharan mineral dust, atmospheric aerosol, lidar, lidar depolarisation technique, planetary boundary layer

1. Introduction

The planetary boundary layer (PBL) is the part of the troposphere directly affected by the surface. A deeper knowledge on the entrainment processes occurring at the top of the PBL is fundamental in aerosol studies, since these processes can transfer aerosol from the free troposphere to surface level. The presence of aerosol particles near the surface is highly relevant as they affect visibility (Prospero, 1999) and may have a negative impact on human health

(e.g., Kwon et al., 2002; Pérez et al., 2008). A better knowledge of these entrainment processes is very important for compliance with the European legislation. For instance, EU Directive 2008/50/EC about air quality specifies the possibility to subtract the contribution of natural sources when reporting the exceedances of air quality standards such as PM_{10} levels (i.e. particles with aerodynamic diameters less than $10 \mu\text{m}$). This is of particular relevance in Southern European countries, which are often affected by North African mineral dust intrusions. This transport of mineral dust typically occurs as advected layers in the free troposphere (Navas-Guzmán et al., 2013) and due to the entrainment and convective processes within the PBL can significantly affect PM_{10} mass concentrations at surface level.

In this study, we used a multiwavelength Raman lidar with depolarisation capabilities in synergetic combination

*Corresponding author.

email: jabravo@ugr.es

†Currently working at CNRM-GAME, Météo-France and EUMETSAT.

Responsible Editor: Kaarle Hämeri, University of Helsinki, Finland.

with a sun-photometer for monitoring the entrainment processes of a lofted Saharan dust layer within the PBL. In-situ instrumentation was used to verify the presence of mineral dust at the surface. Furthermore, in order to estimate the amount of mineral dust at different height levels that was available to be dispersed into the PBL, the dust mass concentration profiles were retrieved by means of the Polarizing Lidar Photometer Networking (POLIPHON) based on lidar depolarisation information (Ansmann et al., 2011; Ansmann et al., 2012). In addition, this method was compared to the coarse mass concentration profiles retrieved with airborne instrumentation.

2. Experimental site

Data used in this study were measured at the Andalusian Institute for Earth System Research (IISTA-CEAMA), located in Granada (37.16°N, 3.61°W, 680 m asl). Granada is a non-industrialised medium-size city surrounded by mountains, with a population of 240 000 inhabitants. The population of the metropolitan area is around 350 000 inhabitants (source: www.ine.es). It is placed in the Southern Iberian Peninsula where continental climate prevails with high temperatures and scarce rainfall during summer and low temperature and moderate rain during winter. Main local aerosol sources are road traffic, soil re-suspension (especially during the warm-dry season) and domestic heating based on fuel-oil combustion during winter (Titos et al., 2012, Titos et al., 2014a). Main external aerosol sources are the Sahara Desert located at 500 km southward as well as industrial and urban areas in Europe (Lyamani et al., 2010).

3. Instrumentation and methodology

3.1. Passive remote sensing instrumentation

Measurements of columnar aerosol properties at daytime were obtained using a CIMEL CE-318 sun-photometer. This instrument is included in the AERONET network (Holben et al., 1998) (www.aeronet.gsfc.nasa.gov), which imposes standardisation of instruments, calibration, processing and data distribution. The sun-photometer provides solar extinction measurements at seven channels ranging from 340 to 1020 nm and sky radiances measured at 440, 675, 870 and 1020 nm. Solar extinction measurements are used to compute the aerosol optical depth (AOD) at 340, 380, 440, 500, 675, 870 and 1020 nm. The AOD_{CIMEL} uncertainty ranges from ± 0.01 in the infrared-visible to ± 0.02 in the ultraviolet channels (Eck et al., 1999). The sky radiance measurements in conjunction with AOD_{CIMEL} data at four wavelengths are used to retrieve aerosol micro-physical properties like columnar aerosol size distribution, refractive index and single scattering albedo, $\omega(\lambda)$, using

the algorithm by Dubovik and King (2000) with improvements by Dubovik et al. (2006). The reported uncertainties for aerosol properties are around 10–35%, for the size distribution retrievals in the $0.1 \mu\text{m} < r < 7 \mu\text{m}$ size range, while for sizes retrieval outside of this range, uncertainties rise up to 80–100% [Dubovik and King (2000); Dubovik et al. (2006)].

In addition, continuous monitoring of tropospheric temperature profiles during the studied period was performed using a ground-based passive microwave radiometer (RPG-HATPRO G2, Radiometer Physics GmbH, Birkenmaarstraße 10, 53340 Meckenheim, Germany). The passive microwave radiometer performs measurements of the sky brightness temperature with a radiometric resolution between 0.3 and 0.4 K root mean square error at 1 s integration time (Navas-Guzman et al., 2014). The radiometer uses direct detection receivers within two bands: 22–31 and 51–58 GHz. The first-band radiation provides information about the tropospheric water-vapour profile, while the second band is related to the temperature profile. Using an inversion algorithm developed by Rose et al. (2005), temperature profiles were retrieved from brightness temperature and surface meteorological data. The accuracy of the temperature is 0.8 K within the first 2 km and 1.2 K at higher altitudes. Tropospheric profiles were obtained from the surface up to 10 km using 39 heights with vertical resolution ranging from 10 m near the surface to 1 km for altitudes higher than 7 km agl. 25 independent points with vertical resolution between 10 and 200 m are provided below 3 km agl, where the PBL is usually located over Granada (Granados-Muñoz et al., 2012). Temperature profiles were used to determine the PBL height using the parcel method (Holzworth, 1964; Granados-Muñoz et al., 2012; Wang et al., 2012; Cimini et al., 2013; Corredor-Ardoy et al., 2014) and to calculate the potential temperature in combination with the vertical profiles of pressure of the 1976 Standard Atmosphere (Krueger and Minzner, 1976) scaled at surface pressure. This method is applied only during daytime since results are not reliable under non-convective conditions. The PBL height uncertainty is around 200 and 400 m above and below 2 km, respectively, due to the aforementioned different resolution of the temperature profile derived by the microwave radiometer (Granados-Muñoz et al., 2012).

The microwave radiometer is complemented with the air temperature data measured at 2 m agl by the meteorological station. Due to the high sensitivity of the parcel method to the temperature near to the surface, the use of the data from the meteorological station provides more accurate results.

3.2. Active remote sensing instrumentation

A multiwavelength Raman lidar model LR331-D400 (Raymetrics, S.A., 32 Spartis, Metamorfosis 14452, Athens,

Greece) was operated pointing to the zenith with emissions at 355, 532 and 1064 nm and detection at elastic and Raman-shifted wavelengths at 355, 532 (parallel and perpendicular components respect to the polarising beam-splitter plane) and 1064 nm, and 387, 408 and 607 nm, respectively. The telescope diameter of the LR331-D400 is 40 cm. In order to correct the overlap deviation in the multiwavelength lidar, we apply the procedure proposed by Wandinger and Ansmann (2002). In most cases, this correction allows the retrieval of the profile at 355 and 532 nm down to 320 m above the station (Navas Guzmán et al., 2011). This lidar system is part of EARLINET (European Aerosol Research Lidar Network) (Pappalardo et al., 2014) and fulfils the quality assurance protocols established by the network. A detailed description of this lidar system is included in Guerrero-Rascado et al. (2009).

Lidar data allows the retrieval of the aerosol-particle backscatter (β) and extinction coefficients (α) as well as the volume linear depolarisation ratio (δ'). β and α were retrieved following the Klett-Fernald (Fernald et al., 1972; Klett, 1981; Fernald, 1984; Klett, 1985) and Raman (Ansmann et al., 1990) methods for daytime and night-time measurements, respectively. During daytime, β derived from lidar measurements requires the assumption of the height-constant extinction-to-backscatter ratio, called lidar ratio (LR). The determination of the LR was performed by matching the integrated extinction coefficient derived by lidar (AOD_{lidar}) and the aerosol optical depth measured by a co-located sun-photometer (AOD_{CIMEL}) accepting a range of variation less than 0.03 (Landulfo et al., 2003). As AOD_{lidar} and AOD_{CIMEL} are obtained at different wavelengths, the AOD_{CIMEL} at 532 nm was calculated by linear interpolation. β and α statistical uncertainties were determined by means of Monte Carlo technique (Pappalardo et al., 2004; Guerrero-Rascado et al., 2009). In this work, the maximum errors of the retrieved β profiles were around 30% at the lowermost part of the profile where the maximum differences between the real and the assumed LR were expected. Typically, relative errors of the aerosol-particle backscatter coefficient derived with Raman and Klett-Fernald method are less than 15 and 20%, respectively, and relative errors of the aerosol-particle extinction coefficient derived with Raman method are in the range 10–30% (Russel et al., 1979; Franke et al., 2001; Alados-Arboledas et al., 2011; Preissler et al., 2011).

The volume linear depolarisation ratio, δ' , (Cairo et al., 1999) was retrieved from the parallel and perpendicular polarised components at 532 nm from the multiwavelength Raman lidar. The depolarisation calibration was obtained using the $\Delta 90^\circ$ calibration method presented by Freudenthaler et al. (2009) and detailed by Bravo-Aranda et al. (2013). δ' uncertainties have been estimated to range

between 0.025 and 0.045 for δ' values of 0.004 and 0.45, respectively (Bravo-Aranda, 2014).

3.3. Ground-based in-situ instrumentation

In-situ aerosol-particle scattering and absorption properties were obtained with an integrating nephelometer (TSI INCORPORATED, 500 Cardigan Road, Shoreview, MN, 55126, USA) and a multi-angle absorption photometer (MAAP, Thermo ESM Andersen Instruments, 81 Wyman Street, Waltham, MA, 02451, USA), respectively. The nephelometer was used to measure the aerosol-particle scattering coefficient, σ_{sp} , at 450, 550 and 700 nm. This instrument is periodically calibrated using CO_2 and filtered air. Additionally, the raw σ_{sp} data are corrected for truncation and non-Lambertian illumination errors using the method described by Anderson and Ogren (1998). The uncertainty in σ_{sp} is of 7% (Heintzenberg et al., 2006). The aerosol-particle absorption coefficient was measured at 637 nm, $\sigma_{\text{ap}}(637 \text{ nm})$, using a MAAP with an estimated uncertainty of 12% (Petzold and Schonlinner, 2004; Petzold et al., 2005). Air sampling for these instruments is obtained from the top of a stainless steel tube of 20 cm diameter and 5 m length (Lyamani et al., 2008, 2010), located at about 15 m above the ground. More details on the instruments and the experimental setup are given by Lyamani et al. (2010).

3.4. Airborne in-situ instrumentation

Airborne measurements were carried out by the INTA (National Institute for Aerospace Technology) CASA C-212-200 atmospheric aircraft over Granada on 27 June 2011. The airborne platform obtained vertical measurements following a pseudo spiral centred at (37.19°N, 3.57°W), 8 km away from the experimental site (37.16°N, 3.61°W), with a diameter of about 4500 m. The aircraft overpassed the lidar system at heights between 1200 and 5200 m asl. Figure 1 shows the ascending track of the INTA-C212–200 aircraft during this flight, which took place around 10:45 UTC (local time: UTC + 2). The aircraft was equipped with two optical particle counters: the PCASP-100X manufactured by Particle Metrics System and the Cloud, Aerosols and Precipitation Sonde (CAPS) from Droplet Measurement Technologies (DMT) (Baumgardner et al., 2001). The latter is composed of multiple sensors but only the cloud aerosol spectrometer with depolarisation (CAS) was used in this work. Both instruments were fixed at two hard points located under the aircraft wings.

CAS probe classifies the particles sizes in the range 0.51–50 μm into 30 channels logarithmically distributed. Its measuring principle is based on light-scattering at 680 nm, i.e. particles scatter light from an incident laser,

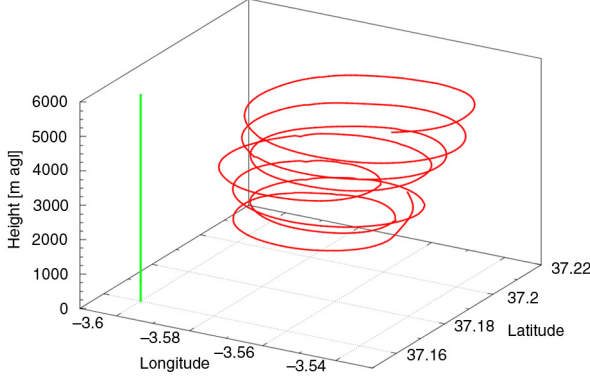


Fig. 1. Ascending track of the INTA C212-200 aircraft during the flight on 27 June 2011 around 10:45 UTC. Green line represents the vertical of CEAMA station.

and collecting optics guide the light scattered in the 4–12 range into a forward-sizing photodetector. This light is measured and used to infer particle size. The uncertainty of this probe varies between 15 and 20% for the size distributions (Baumgardner et al., 2001; Feingold et al., 2006).

The PCASP-100X (passive cavity aerosol spectrometer probe) provides size distributions of aerosol particles in the range 0.1–3 μm of diameter in 15 bins. The measuring principle is the same to the CAS. The scattered radiation between 35 and 135 degrees is collected to determine the size. The wavelength of the laser is 632.8 nm. Size distributions are provided with an uncertainty of 20% (Baumgardner et al., 2005).

Volume concentration profiles for the fine mode (radius between 0.05 and 0.5 μm) and coarse mode (radius from 0.5 to 25 μm) were obtained from the PCASP-100X and CAS sondes, respectively. A refractive index correction is applied to retrieve aerosol volume concentrations since polystyrene latex spheres and glass beads with refractive indices (from 1.51 to 1.56) different to that of the atmospheric aerosols were used for calibration. In order to retrieve the mass concentration profile from the volume concentration profile, aerosol particles were considered as spheres of density 2.6 $\text{g}\cdot\text{cm}^{-3}$ for Saharan mineral dust (Perez et al., 2006).

3.5. Derived aerosol-particle properties

From the aerosol properties measured with the aforementioned instrumentation, some other optical and physical properties were calculated as indicated in Table 1. The AOD-related Angström exponent at wavelengths λ_1 and λ_2 , $\hat{a}_{AOD}(\lambda_1, \lambda_2)$, provides information about the wavelength dependence of AOD [eq. (1)]. Similarly, different Angström exponents $\hat{a}(\lambda_1, \lambda_2)$ related to β , α , and σ_{sp} with different combinations of λ_1 and λ_2 are defined [eqs. (2) and (3)]. The Angström exponent increases with decreasing contribution of coarse particles in the aerosol mixture and takes values around 2 when the scattering/absorption process is dominated by fine particles, while it is close to 0 when the scattering/absorption process is dominated by coarse particles (Seinfeld and Pandis, 1998; Schuster et al., 2006). Single scattering albedo was retrieved using eq. (4) at 637 nm.

Table 1. Aerosol-particle optical and physical properties calculated from optical properties

Property	Symbol/Equation
AOD-related Angström exponent	$\hat{a}_{AOD}(440, 870\text{nm}) = -\frac{\ln(AOD(440)/AOD(870))}{\ln(440/870)}$ (1)
σ_{sp} -related Angström exponent	$\hat{a}_{\sigma}(450, 700\text{nm}) = -\frac{\ln(\sigma_{sp}(450)/\sigma_{sp}(700))}{\ln(450/700)}$ (2)
α , β -related Angström exponent	$\hat{a}_{\alpha,\beta}(352, 532\text{nm}) = -\frac{\ln(\alpha, \beta(355)/\alpha, \beta(532))}{\ln(355/532)}$ (3)
Single scattering albedo	$\omega(\lambda) = -\frac{\sigma_{sp}(\lambda)}{\sigma_{sp}(\lambda) + \sigma_{ap}(\lambda)}$ (4)
AOD _{PBL}	$\int_0^{z_{PBL}} \alpha(z) dz \equiv \int_0^{z_{PBL}} \beta(z) LR dz$ (5)
AOD _{FT}	$\int_{z_{PBL}}^{z_{ref}} \alpha(z) dz \equiv \int_{z_{PBL}}^{z_{ref}} \beta(z) LR dz$ (6)
Lidar ratio	$LR(\lambda) = \frac{\alpha(\lambda)}{\beta(\lambda)}$ (7)
Particle linear depolarisation ratio	$\delta^p = \frac{\delta'(1+\delta^m)R - \delta^m(1+\delta')}{(1+\delta^m)R - (1+\delta')}$ (8)
β_{dust}	$\beta_{dust} = \beta \cdot \frac{\delta^p(1-\delta_{dust}^p)(1-\delta_{aer}^p)}{(\delta_{dust}^p - \delta_{aer}^p)(1-\delta^p)}$ (9)
m_{dust}	$m_{dust} = \rho_{dust} \frac{C_{dust}}{AOD_{dust}} \beta_{dust} LR_{dust}$ (10)

The PBL and FT contribution to the AOD, AOD_{PBL} [eq. (5)] and AOD_{FT} [eq. (6)], respectively, were retrieved by integrating the lidar extinction coefficient between the boundaries indicated in Table 1, using a similar procedure to the one applied to calculate the AOD_{lidar} .

The night-time LR profiles at 355 and 532 nm were calculated as the ratio between the Raman-retrieved extinction and backscatter coefficients [eq. (7) from Table 1]. This property depends on the size distribution, refractive index, wavelength, relative humidity and particle shape (Mishchenko et al., 1997; Ackermann, 1998). Large LR values are associated with highly light absorbing particles while low LR values are indicative of scattering particles (Muller et al., 2003; Navas-Guzmán et al., 2013).

Particle linear depolarisation ratio (δ^p) was retrieved from the δ' and the particle-to-molecular backscatter coefficients ratio, R , called backscattering ratio [eq. (8)]. δ' shows the depolarisation caused by both molecules and aerosol particles, whereas δ^p only describes the depolarisation caused by aerosol particles providing information about the aerosol-particle shape. Large δ^p values are related to non-spherical particles, whereas low δ^p values are related to spherical particles (Freudenthaler et al., 2009). δ^p varies between 0.01 for sulphates and 0.35–0.4 for ash (Ansmann et al., 2011). The uncertainty of δ^p was estimated between 10 and 25% according to Freudenthaler et al. (2009).

The anthropogenic and mineral dust aerosol contribution to β was separated based on the work of Shimizu et al. (2004). This method can be used to separate aerosol-particle contribution with different depolarising capabilities.

The dust backscatter coefficient, β_{dust} , is calculated using eq. (9) where the height and spectral dependence was omitted for simplicity. δ^p_{dust} and δ^p_{ant} represent δ^p values for pure dust and for the anthropogenic aerosol, respectively. A δ^p_{dust} value of 0.31 ± 0.10 was chosen according to the results of SAMUM campaign (Freudenthaler et al., 2009). The δ^p_{ant} value was calculated for the study area obtaining a value of 0.05 ± 0.02 for situations dominated by anthropogenic conditions, similar to that used by Nemuc et al. (2013) of 0.03. Using these values, the dust mass concentrations, m_{dust} , is retrieved using POLIPHON method (Ansmann et al., 2011, 2012). POLIPHON is based on the combination of lidar depolarisation and sun-photometer measurements as indicated in eq. (10), where ρ_{dust} and LR_{dust} are the particle mass density and the dust LR, respectively. For pure dust particles, $\rho_{dust} = 2.6 \text{ g} \cdot \text{cm}^{-3}$ (Perez et al., 2006) and a value of $LR_{dust} = 42 \pm 6 \text{ sr}$ was used, obtained from the Raman retrieval in the period 00:00–01:00 on 27 June (Fig. 2). The ratio C_{dust}/AOD_{dust} , called mean extinction-to-mass conversion factor, represents the ratio of column-integrated coarse volume concentration (C_{dust}) to AOD for the coarse (dust) mode (AOD_{dust}). C_{dust} was calculated from AERONET-derived level 1.5 inversion products on 27 June 2011 at 11:19 UTC (local time: UTC+2). AOD_{dust} was derived using the total AOD at 532 nm and the fine fraction η , provided by AERONET (O'Neill et al., 2001a, b). By applying the law of error propagation to eq. (10), the uncertainty in the mass concentration was estimated to be about 45%, considering the following individual uncertainties: 25% for the mass densities, 20% for the dust LR, backscatter coefficient

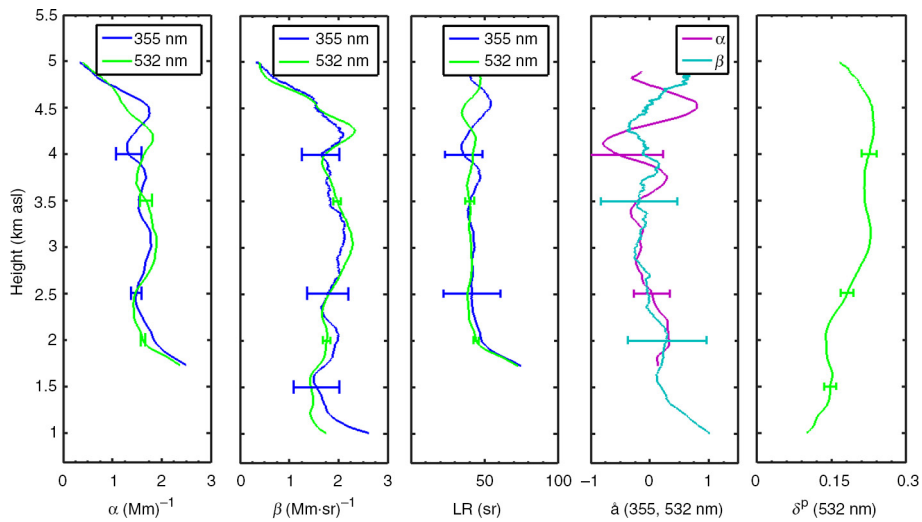


Fig. 2. From left to right, aerosol extinction (α) and backscattering (β) coefficients and lidar ratio (LR) at 355 and 532 nm, backscatter- and extinction-related Angström exponent [$\hat{a}_\beta(355, 532 \text{ nm})$ and $\hat{a}_\alpha(355, 532 \text{ nm})$, respectively] and particle linear depolarisation ratio, $\delta^p(532 \text{ nm})$, at 00:00–01:00 UTC on 27 June 2011.

and the linear particle depolarisation ratios, and 15% for the mean extinction-to-mass conversion factors (Ansmann et al., 2011).

4. Results and discussions

4.1. Night-time conditions

Raman lidar measurements during the night on 27 June 2011 were analysed in order to characterise the aerosol type and its vertical structure. Figure 2 shows α , β and LR at 355 and 532 nm retrieved by Raman inversion, $\hat{\alpha}_\beta(355, 532 \text{ nm})$, $\hat{\alpha}_\beta(355, 532 \text{ nm})$ and $\delta^P(532 \text{ nm})$ profiles at 00:00–01:00 UTC 27 June 2011 (local time: UTC + 2). $\hat{\alpha}_\beta$ and δ^P profiles exhibit two well-differentiated regions: the upper region corresponds to a layer from 3 to 5 km asl, with mean and standard deviations of -0.02 ± 0.25 for $\hat{\alpha}_\beta$ and 0.26 ± 0.05 for δ^P , whereas the lower region (1–3 km asl) is characterised by a negative correlation between $\hat{\alpha}_\beta$ and δ^P , with decreasing values of $\hat{\alpha}_\beta$ (1.00–0.23) and increasing values of δ^P (0.12–0.26) with height. This behaviour indicates a gradual increase of the predominance of coarse and non-spherical particles with height in this region (Fig. 2), suggesting an increase in the presence of mineral dust.

The values of $\hat{\alpha}_\beta$ and δ^P in the upper region are in agreement with the values of $\hat{\alpha}_\beta$ (355, 532 nm) and $\delta^P(532 \text{ nm})$ measured by Tesche et al. (2009) and Freudenthaler et al. (2009) for pure Saharan mineral dust (0.19 ± 0.20 and

0.31 ± 0.03 , respectively). The LR mean values and standard deviations at 355 and 532 nm of the upper layer obtained here are 43 ± 5 and $41 \pm 3 \text{ sr}$, respectively. These values are in the range of values provided in previous studies for medium-transport dust events (Guerrero-Rascado et al., 2009; Müller et al., 2009; Preissler et al., 2011; Bravo-Aranda et al., 2013; Preissler et al., 2013). Considering the error bars, the measured values of LR at 355 and 532 nm are in the range 53 ± 7 and $55 \pm 7 \text{ sr}$ for pure Saharan mineral dust presented by Tesche et al. (2009).

In order to confirm the presence of Saharan dust over Granada on 27 June, as indicated by the experimental results, 5-day backward trajectories at 00:00 and 13:00 UTC on 27 June ending at Granada are shown in Fig. 3. The backward trajectories were computed with the HYSPLIT model (Draxler and Rolph, 2014) and using the GDAS database. The air masses came from the North of Africa at 2500, 3500, 4500 and 6000 m agl. Particularly, the 4000 m agl backward trajectory comes across the Saharan Desert at heights lower than 1000 m agl between 19 and 22 June and therefore it is very likely to be loaded with mineral dust.

4.2. Mixing process: downward entrainment of the mineral dust into the PBL

Figure 4 shows the temporal evolution of the range corrected signal at 532 nm, $\text{RCS}(532 \text{ nm})$, the PBL height and the total $\text{AOD}_{\text{CIMEL}}(532 \text{ nm})$, AOD_{PBL} and AOD_{FT}

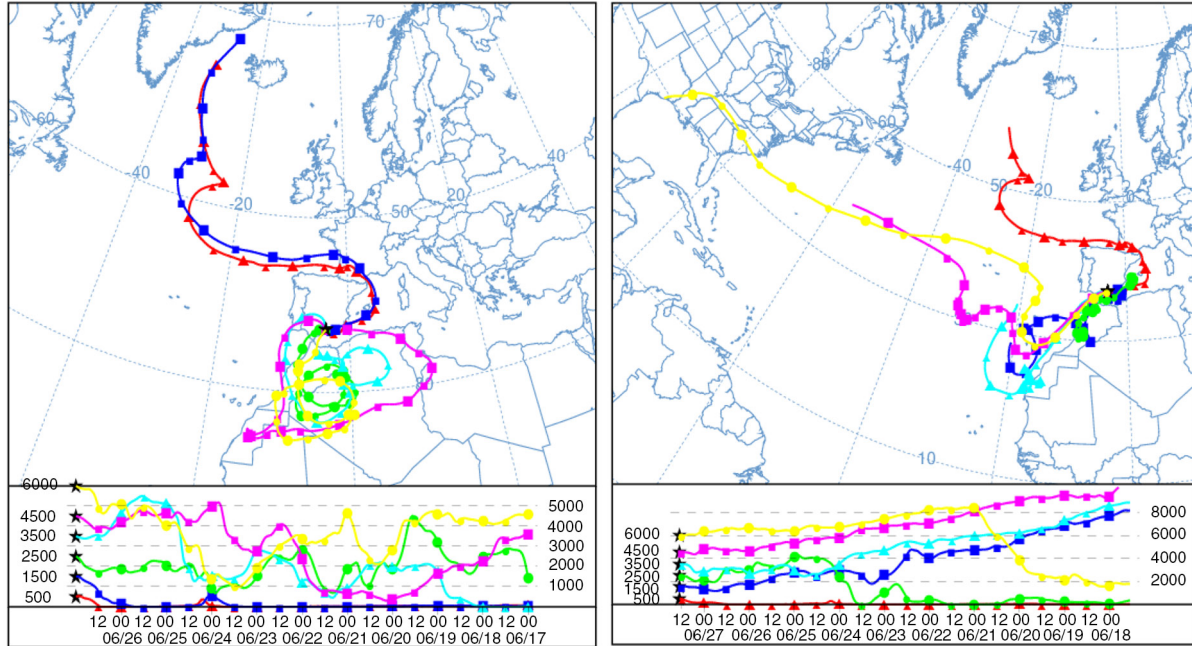


Fig. 3. HYSPLIT backward trajectories ending at 00:00 (left) and at 13:00 UTC (right) on 27 June 2011 at 500, 1500, 2500, 3500, 4500 and 6000 m agl (Granada, 37.16°N, 3.61°W).

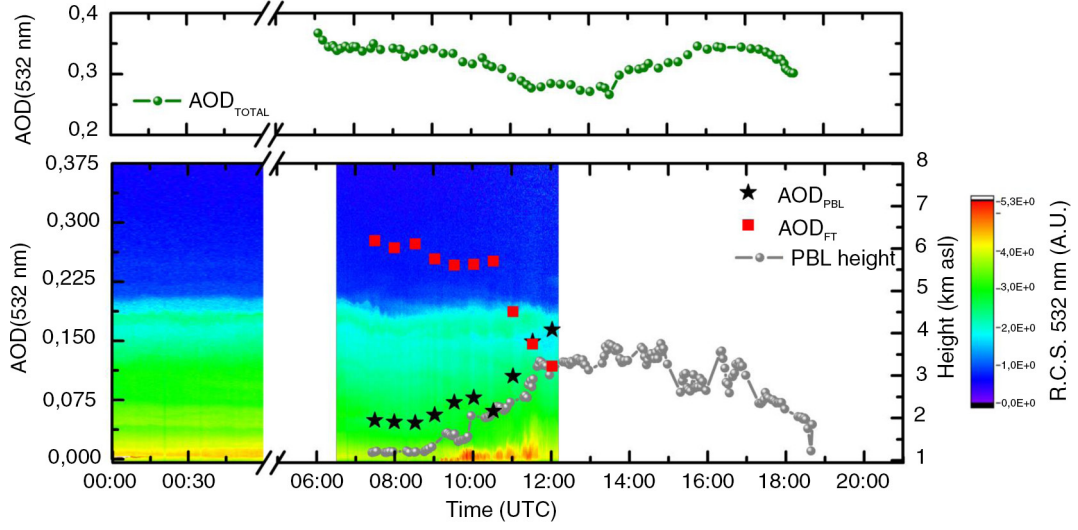


Fig. 4. Top: temporal evolution of the total AOD at 532 nm (green). Bottom: temporal evolution of PBL height (grey) and the PBL and FT contribution to AOD(532 nm) (black and red, respectively) on 27 June 2011. Colour maps represent the lidar range corrected signal at 532 nm on 27 June 2011 from 00:00 to 01:00 and 06:30 to 12:15 UTC.

obtained on 27 June 2011. The temporal evolution of the RCS(532 nm) shows a similar aerosol-load structure at night- and daytime within the first 4.5 km. $AOD_{CIMEL}(532 \text{ nm})$ is rather stable (~ 0.28) along daytime, whereas AOD_{PBL} and AOD_{FT} change during the morning: AOD_{PBL} increases from 15% at 07:30 UTC up to 58% at 12:00 UTC, whereas AOD_{FT} decreases from 85% down to 42% during the same period. The aerosol-load vertical structure changes along the morning in coincidence with a great enhancement of the PBL height as it can be seen in Fig. 4.

Figure 5 shows the hourly mean potential temperature (θ) profiles between 07:30 and 11:30 UTC. The large increase of θ at surface level and the evolution of θ profiles are coherent with the PBL heights obtained with the parcel method. The superadiabatic behaviour close to the surface (680–690 m asl), with $\partial\theta/\partial z < 0$, together with the increase in the atmospheric instability in the layer 690–1490 m asl during the morning, leads to an increase of the convective activity. These convective processes result in variations of AOD_{FT} and AOD_{PBL} due to mineral dust entrainment from the FT to the PBL. Similar phenomena were detected in Cape Verde Island by Engelmann et al. (2011) where a vertical mixing between air masses in the PBL and the FT was detected.

The mineral dust entrainment from the FT to the PBL is also clearly evidenced by the temporal evolution of $\hat{\alpha}_\beta$, δ^P and β_{dust}/β profiles. Figure 6 shows the β , $\hat{\alpha}_\beta$, δ^P and β_{dust}/β profiles from 07:30 to 11:30 UTC (local time: UTC + 2) up to 2.5 km asl. As it can be seen, β presents slight variations in the lowermost part of the profile during the morning, whereas $\hat{\alpha}_\beta$ and δ^P show higher variability with time. This

temporal evolution suggests that the dust particles arriving at higher levels (above 2 km) are getting incorporated into the lower layers of the atmosphere. Thus, at 11:30 local time $\hat{\alpha}_\beta$ and δ^P values at the lowermost part of the profile are similar to those found above 2 km. Table 2 shows the mean values of $\delta^P(532 \text{ nm})$, $\hat{\alpha}_\beta(355, 532 \text{ nm})$ and β_{dust}/β in the range 1–1.1 km asl and the values of the $\hat{\alpha}_{sp}(450, 700 \text{ nm})$ at surface and the PBL height at 07:30 and

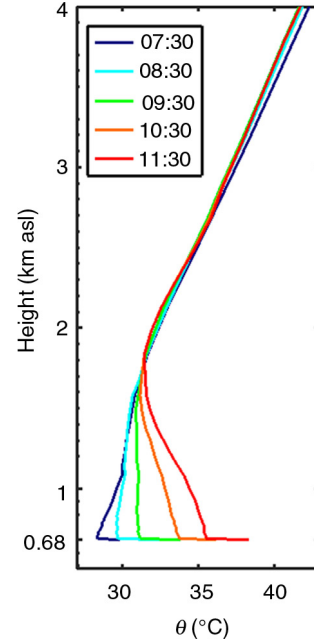


Fig. 5. Hourly mean potential temperature evolution at different hours showed by the label (UTC) on 27 June 2011.

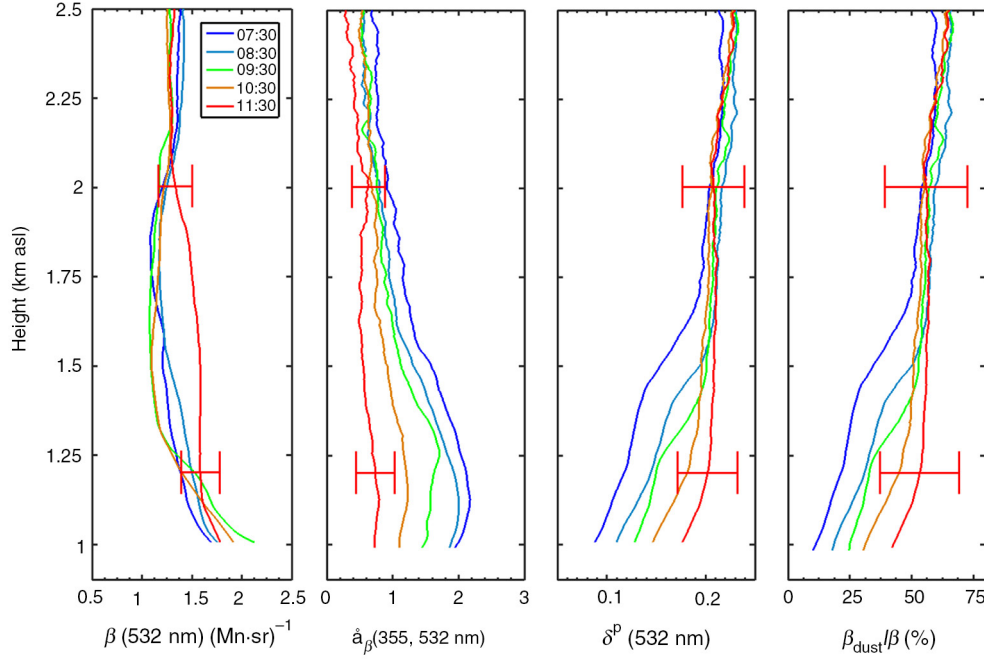


Fig. 6. $\beta(532 \text{ nm})$, $\hat{a}_\beta(355, 532 \text{ nm})$, $\delta^P(532 \text{ nm})$ and $\beta_{\text{dust}}/\beta(\%)$ profiles retrieved using 30-min averaged lidar signals at different hours following the label (UTC) on 27 June 2011. Only error bars corresponding to 11:30 UTC are shown for clarity.

11:30 UTC. As can be seen, \hat{a}_β and δ^P present an opposite trend with decreasing \hat{a}_β and increasing δ^P values and $\beta_{\text{dust}}/\beta$ between 07:30 and 11:30 UTC. This behaviour linked to the increase of the PBL height points to a downward entrainment of the dust into the PBL due to the convective processes. To the best of our knowledge, the combined information provided by \hat{a}_β and $\beta_{\text{dust}}/\beta$ profiles is used here for the first time to study the entrainment and mixing processes within the PBL.

In order to discard that the increase of mineral dust could be related to local sources or to advected mineral dust at low levels additional data are used. δ^P value measured on 27 June 2011 is compared to a reference measurement on 14 June in absence of transported mineral dust. δ^P is almost twice on 27 June 2011 (~ 0.19) compared to 14 June 2011 (~ 0.10) in the lowermost layer. Thus, the large

difference of δ^P near the surface between 27 and 14 June shows that the presence of the mineral dust in the PBL on 27 June 2011 cannot be solely due to local mineral sources. On the other hand, Fig. 3 shows that the air masses at 500 m agl came from Europe across the Mediterranean basin indicating that the increase of mineral dust at low altitudes is not related to Saharan dust intrusion at this level.

Figure 7a and 7b show the temporal evolution of $\sigma_{\text{sp}}(550 \text{ nm})$, $\sigma_{\text{ap}}(637 \text{ nm})$, $\hat{a}_{\text{sp}}(450, 700 \text{ nm})$ and $\omega(637 \text{ nm})$ at surface level from in-situ measurements on 27 June 2011 as well as the typical conditions at the station for working days not affected by Saharan mineral dust on June. The temporal resolution on 27 June ranges between 1 and 15 minutes depending on the instrument, whereas June average values correspond to 15 minutes intervals. Shaded regions in Fig. 7 indicate the standard deviation. In Fig. 7a, it can be seen that $\hat{a}_{\text{sp}}(450, 700 \text{ nm})$ values range between 0.8 and 1.5 on 27 June while the June monthly mean $\hat{a}_{\text{sp}}(450, 700 \text{ nm})$ values range between 1.5 and 1.8. It indicates a larger predominance of coarse particles on 27 June compared to typical conditions, related to the presence of mineral dust at surface. During night-time, $\hat{a}_{\text{sp}}(450, 700 \text{ nm})$ and $\omega(637 \text{ nm})$ values are larger than their mean values in June (Fig. 7a), indicating the presence of mineral dust also during night-time. Even though mineral dust is detected at the surface from night-time, a significant change of $\omega(637 \text{ nm})$ and $\hat{a}_{\text{sp}}(450, 700 \text{ nm})$ is detected

Table 2. Thirty-minute mean and standard deviation of in-situ and lidar optical properties at surface and between 1 and 1.1 km asl, respectively, and the PBL height at two different hours during the morning of 27 June 2011

Property	07:30 UTC	11:30 UTC
$\delta^P(532 \text{ nm})[1-1.1 \text{ km}]$	0.08 ± 0.02	0.19 ± 0.03
$\hat{a}_\beta(355, 532 \text{ nm})[1-1.1 \text{ km}]$	2.1 ± 0.1	0.8 ± 0.1
$\beta_{\text{dust}}/\beta[1-1.1 \text{ km}](\%)$	12 ± 10	45 ± 10
PBL height (km asl)	1.2 ± 0.05	2.8 ± 0.1
$\hat{a}_{\text{sp}}(450, 700 \text{ nm})$	1.23 ± 0.05	0.86 ± 0.05

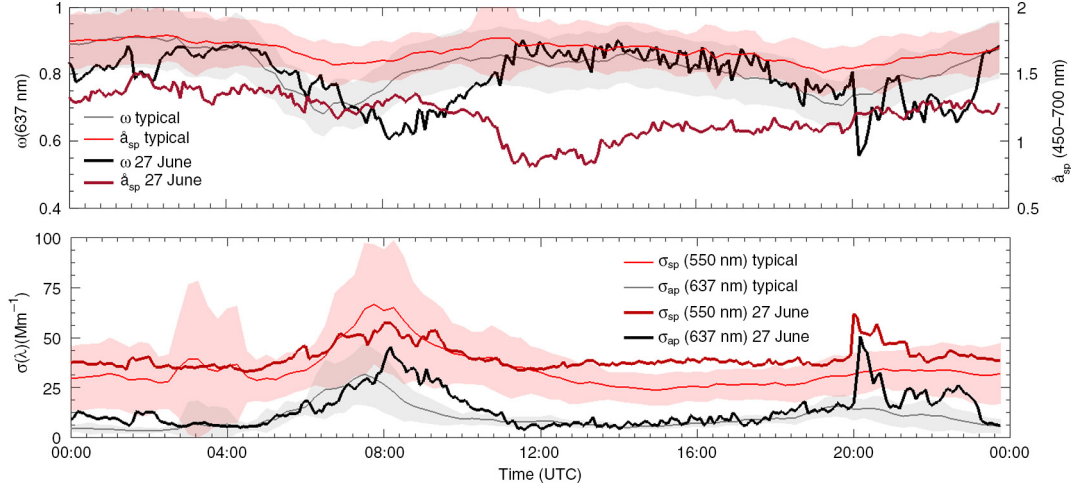


Fig. 7. Temporal evolution of in-situ properties: (a) $\hat{a}_{sp}(450, 700 \text{ nm})$, $\omega(637 \text{ nm})$ and (b) $\sigma_{sp}(550 \text{ nm})$, $\sigma_{ap}(637 \text{ nm})$. Thick lines correspond to data on 27 June and thin lines correspond to the mean of June 2011 for working days not affected by Saharan mineral dust at surface level. Shaded regions indicate the standard deviation.

around 11:30 UTC. At this time, an increase of $\omega(637 \text{ nm})$ and a decrease of $\hat{a}_{sp}(450, 700 \text{ nm})$ at surface level occur in coincidence with the decrease of $\hat{a}_{\beta}(355, 532 \text{ nm})$ and the increase of β_{dust}/β values in the lowest part of the atmospheric column. As it can be seen in Table 2, $\hat{a}_{\beta}(355, 532 \text{ nm})$ in the range 1–1.1 km asl and $\hat{a}_{sp}(450, 700 \text{ nm})$ decrease from 07:30 to 11:30 UTC indicating a larger predominance of coarse particles. The agreement between the temporal evolution of $\hat{a}_{\beta}(355, 532 \text{ nm})$ at 1 km asl and $\hat{a}_{sp}(450, 700 \text{ nm})$ at surface is related to the strong convective processes which facilitate the mixing of anthropogenic particles originated close to the surface and the mineral dust located at higher altitudes. Additionally, as Fig. 7b shows, the trend of $\sigma_{sp}(550 \text{ nm})$ values between morning peak and the afternoon plateau points to this hypothesis. $\sigma_{sp}(550 \text{ nm})$ mean values for June on working days not affected by Saharan dust events decrease from 63 Mm^{-1} at 08:00 UTC to 25 Mm^{-1} at 13:00 UTC, due to the increasing PBL height and decreasing road traffic emissions. However, on 27 June, $\sigma_{sp}(550 \text{ nm})$ values show a less intense decrease from 57 Mm^{-1} (08:00 UTC) to 37 Mm^{-1} (13:00 UTC) likely connected to the entrainment of mineral dust within the PBL.

The diurnal evolution of in-situ aerosol properties at surface is affected by the presence of mineral dust. Maxima of $\sigma_{sp}(550 \text{ nm})$ and $\sigma_{ap}(637 \text{ nm})$ in June occur at 07:30 and 07:45 UTC, respectively, whereas the minimum of $\omega(637 \text{ nm})$ occurs at 06:30 UTC (Fig. 7). Thus, a temporal displacement of $\sigma_{sp}(550 \text{ nm})$ and $\sigma_{ap}(637 \text{ nm})$ maxima is observed under typical conditions (Lyamani et al., 2010). This effect was previously detected by Lyamani et al. (2010) and explained in terms of the time required for secondary

particle formation by gas-to-particle conversion. However, this temporal displacement is not observed on 27 June since maxima of $\sigma_{sp}(550 \text{ nm})$ and $\sigma_{ap}(637 \text{ nm})$ and minimum of $\omega(637 \text{ nm})$ are coincident at 08:00 UTC. A possible explanation for this behaviour could be, among other factors, the presence of mineral dust particles at surface level that favour gaseous deposition and can suppress or reduce gas-to-particle conversion processes. Thus, the entrainment of mineral dust into the PBL can significantly influence the internal mixing and particle formation processes occurring within the PBL.

4.3. Estimation of mass concentration profiles

According to the air quality report of June 2011 (Andalusian Regional Government, www.juntadeandalucia.es/temas/medio-ambiente.html), on 27 June the PM_{10} daily limit of $50 \mu\text{g}\cdot\text{m}^{-3}$ is exceeded and listed as harmful for human health. On this date, it is observed that convective and entrainment processes incorporate aerosol particles within the PBL from the advected mineral dust layer at higher altitudes increasing the dust mass concentration, m_{dust} , at surface level. Therefore, an estimation of the vertically resolved m_{dust} would help to evaluate the amount of mineral dust available to be incorporated into the PBL. To this aim, POLIPHON (Ansmann et al., 2011; 2012) is used to separate the mineral dust contribution from the urban-dust mixture. The m_{dust} profile at 10:30 UTC derived from POLIPHON is presented together with the coarse-mode mass concentration profile, m_c , derived from airborne data at 10:45 UTC (Fig. 8). As shown in Fig. 8, the dust mass concentration is in the range $30\text{--}60 \mu\text{g}\cdot\text{m}^{-3}$

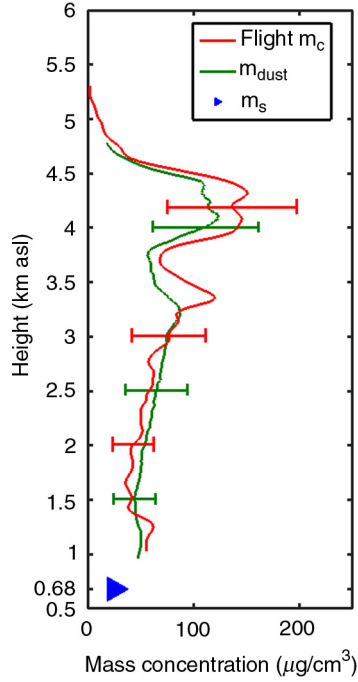


Fig. 8. Dust mass concentration (m_{dust}) retrieved by POLIPHON at 10:30 UTC, coarse-mode mass concentration (m_c) derived from airborne measurements at 10:45 UTC and mean mass concentration of particles with diameters between 1 and $10\ \mu\text{m}$ (m_s) ($\mu\text{g}/\text{m}^3$) in the period 10:00–11:00 UTC at surface level (0.68 km asl) on 27 June 2011.

between 1 and 2 km asl, whereas the mass concentration of particles with diameters in the range $1\text{--}10\ \mu\text{m}$ at surface is $25.5 \pm 1.5\ \mu\text{g}\cdot\text{m}^{-3}$ as measured with a DustTrak DRX (TSI INCORPORATED, 500 Cardigan Road, Shoreview, MN, 55126, USA) (Kim et al., 2004). These results show a larger aerosol-particle load at high altitude than at surface level. Thus, due to convection processes, the coarse mass concentration at surface level could increase leading to the exceedance of the PM_{10} daily limit established by the European Directive observed on this day.

The vertical distribution of the aerosol load determined by lidar and airborne in-situ measurements generally agrees with differences between m_{dust} and m_c lower than 30% in the height ranges 1–2.4 and 3–5 km asl (Fig. 8). In the range 2.4–2.7 km asl, the lidar and the airborne in-situ instrumentation detect maximum peaks at different heights (3.2 and 3.35 km asl, respectively). The difference between the maximum values at these peaks is also around 30%. The differences found between m_{dust} and m_c can be due to the fact that the distance between the lidar station and the aircraft path was around 8 km. In addition, POLIPHON includes assumptions such as the external mixing, the height-constant LR used to retrieve the β profile and the cor-

respondence of the mineral dust with the coarse-mode particles. Furthermore, measurement techniques are different and m_c is retrieved assuming spherical particles which, according to Ginoux (2003), may introduce large uncertainty for particles between 3 and $8\ \mu\text{m}$ of radius. Discrepancies between in-situ and remote sensing data due to hygroscopic growth are not expected in this study since this effect can be neglected for relative humidity values below 40% (region below 3 km asl). In the dust layer, where the relative humidity reaches values around 55%, the hygroscopic enhancement is also negligible since dust particles have low hygroscopicity (Fierz-Schmidhauser et al., 2010; Titos et al., 2014b). The comparison of POLIPHON retrievals with the aircraft measurements shows that this method is appropriate to retrieve the mass concentration of an urban-dust mixture despite of the required assumptions. It is worthy to note that, to our knowledge, this is the first time that POLIPHON method is validated using aircraft measurements.

5. Conclusions

In this work, we use data collected during a Saharan dust outbreak on 27 June 2011. For this day, all the available instrumentation at IISTA-CEAMA station was operating and there was additional information from in-situ instrumentation on-board an aircraft. Data collected during this campaign are used to study mineral dust entrainment processes in the PBL. The synergetic use of active and passive remote sensing instrumentation allowed us to study the interaction between the dust layer located in the FT and the PBL due to the entrainment and convective processes. For this purpose, an approach based on the combined analysis of the temporal evolution of \hat{a}_β and δ^p and β_{dust}/β profiles was used. Up to our knowledge, this kind of approach has not been presented in previous studies. The results obtained evidenced the entrainment of mineral dust within the PBL and an increase of the mineral dust presence at lower levels throughout the morning on 27 June. Additionally, the temporal evolution of the FT and the PBL contribution to the total AOD showed an increase of the PBL contribution to the total AOD, whereas the FT contribution decreased. This indicates that the convective processes enhanced the PBL which ‘trapped’ the dust layer, accelerating the downward dust entrainment. The increase of β_{dust}/β at 1 km asl from $12 \pm 10\%$ to $45 \pm 10\%$ throughout the morning indicates the relevance of this process for the downward entrainment. This work shows the importance of high spatio-temporal resolution measurements for monitoring and analysing aerosol mixing processes.

The temporal evolution of properties derived from in-situ data and lidar depolarisation and backscatter-related

Angström exponent profiles demonstrated that the downward dust entrainment caused an increase of the mineral dust presence at surface level. Furthermore, the delay between aerosol scattering and absorption coefficient at the surface level disappeared, suggesting that the gas-to-particle conversion may be less important due to the gas deposition on particles surface under mineral dust presence at surface level.

In addition, the dust mass concentration was obtained by POLIPHON and, for the first time, compared to the coarse-mode mass concentration retrieved with airborne in-situ measurements. Considering the shortcomings of both methodologies, a relative good agreement (differences below 30%) was obtained. According to the results, POLIPHON is a promising tool to retrieve dust mass concentration profiles in anthropogenic-dust aerosol mixtures and can be used to estimate the amount of mineral dust available to be dispersed into the PBL due to convective activity.

6. Acknowledgements

This work was supported by the Andalusia Regional Government through projects P12-RNM-2409 and P10-RNM-6299, by the Spanish Ministry of Science and Technology through projects CGL2010-18782 and CGL2013-45410-R, and by the EU through ACTRIS project (EU INFRA-2010-1.1.16-262254). CIMEL Calibration was performed at the AERONET-EUROPE calibration centre, supported by ACTRIS [European Union Seventh Framework Program (FP7/2007–2013)] under grant agreement no. 262254. The authors gratefully acknowledge the NOAA Air Resources Laboratory (ARL) for the provision of the HYSPLIT transport and dispersion model and/or READY website (www.ready.noaa.gov). Also, the authors acknowledge images from the BSC-DREAM8b (Dust REgional Atmospheric Model) model, operated by the Barcelona Supercomputing Center (www.bsc.es/projects/earthscience/BSC-DREAM/). Air quality report of June was provided as a result of the Administration Assignment Agreement between the Ministry of Agriculture, Food and Environment and the Superior Council for Scientific Research National Agency for the performance of work related to the study and evaluation of air pollution by particulate matter and metals in Spain. Thanks are also due to INTA Aerial Platforms, a branch of the Spanish ICTS program, and the Spanish Air Force for their efforts in maintaining and operating the aircraft. This work was supported by the University of Granada through the contract ‘Plan Propio. Programa 9. Convocatoria 2013’. Dr. Bravo-Aranda was funded under the grant AP2009-0559. Data supporting this article are available upon request through the corresponding author.

References

- Ackermann, J. 1998. The extinction-to-backscatter ratio of tropospheric aerosol: a numerical study. *J. Atmos. Ocean. Tech.* **15**, 1043–1050.
- Alados-Arboledas, L., Müller, D., Guerrero-Rascado, J. L., Navas-Guzmán, F., Pérez-Ramírez, D. and Olmo, F. J. 2011. Optical and microphysical properties of fresh biomass burning aerosol retrieved by Raman lidar, and star- and sun-photometry. *Geophys. Res. Lett.* **38**, DOI: 10.1029/2010GL045999, 2011.
- Anderson, T. L. and Ogren, J. A. 1998. Determining aerosol radiative properties using the TSI 3563 integrating nephelometer. *Aerosol Sci. Tech.* **29**, 57–69.
- Ansmann, A., Riebesell, M. and Weitkamp, C. 1990. Measurement of atmospheric aerosol extinction profiles with a Raman lidar. *Opt. Lett.* **15**, 746–748.
- Ansmann, A., Tesche, M., Seifert, P., Gross, S., Freudenthaler, V. and co-authors. 2011. Ash and fine-mode particle mass profiles from EARLINET-AERONET observations over central Europe after the eruptions of the Eyjafjallajökull volcano in 2010. *J. Geophys. Res.-Atmos.* **116**, D00U02.
- Ansmann, A., Seifert, P., Tesche, M. and Wandinger, U. 2012. Profiling of fine and coarse particle mass: case studies of Saharan dust and Eyjafjallajökull/Grimsvötn volcanic plumes. *Atmos. Chem. Phys.* **12**, 9399–9415. DOI: 10.5194/acp-12-9399-2012.
- Baumgardner, D., Jonsson, H., Dawson, W., O'Connor, D. and Newton, R. 2001. The cloud, aerosol and precipitation spectrometer: a new instrument for cloud investigations. *Atmos. Res.* **59**, 251–264.
- Baumgardner, D., Raga, G. B., Jimenez, J. C. and Bower, K. 2005. Aerosol particles in the Mexican East Pacific – part I: processing and vertical redistribution by clouds. *Atmos. Chem. Phys.* **5**, 3081–3091.
- Bravo-Aranda, J. A., Navas-Guzman, F., Guerrero-Rascado, J. L., Perez-Ramirez, D., Granados-Muñoz, M. J. and co-authors. 2013. Analysis of lidar depolarization calibration procedure and application to the atmospheric aerosol characterization. *Int. J. Remote Sens.* **34**, 3543–3560.
- Bravo-Aranda, J. A. 2014. *Lidar Depolarization Technique: Assessment of Hardware Polarizing Sensitivity and Applications*. Granada: University of Granada, 284 pp. Online at: <http://hdl.handle.net/10481/34131>
- Cairo, F., Di Donfrancesco, G., Adriani, A., Pulvirenti, L. and Fierli, F. 1999. Comparison of various linear depolarization parameters measured by lidar. *Appl. Opt.* **38**, 4425–4432.
- Cimini, D., De Angelis, F., Dupont, J. C., Pal, S. and Haeffelin, M. 2013. Mixing layer height retrievals by multi-channel microwave radiometer observations. *Atmos. Meas. Tech.* **6**, 2941–2951.
- Corredor-Ardoy, J. L., Bravo-Aranda, J. A., Granados-Muñoz, M. J., Guerrero-Rascado, J. L., Fernández-Gálvez, J. and co-authors. 2014. Active and passive remote sensing for monitoring the planetary boundary layer height. *Óptica Pura y Aplicada* **47**, 83–90.
- Draxler, R. R. and Rolph, G. D. 2014. HYSPLIT (HYbrid Single-Particle Lagrangian Integrated Trajectory) Model access via

- NOAA ARL READY. NOAA Air Resources Laboratory, Silver Spring, MD. Online at: <http://ready.arl.noaa.gov/HYSPLIT.php>.
- Dubovik, O. and King, M. D. 2000. A flexible inversion algorithm for retrieval of aerosol optical properties from sun and sky radiance measurements. *J. Geophys. Res. Atmos.* **105**, 20673–20696.
- Dubovik, O., Sinyuk, A., Lapyonok, T., Holben, B. N., Mishchenko, M. and co-authors. 2006. Application of spheroid models to account for aerosol particle nonsphericity in remote sensing of desert dust. *J. Geophys. Res.-Atmos.* **111**.
- Eck, T. F., Holben, B. N., Reid, J. S., Dubovik, O., Smirnov, A. and co-authors. 1999. Wavelength dependence of the optical depth of biomass burning, urban, and desert dust aerosols. *J. Geophys. Res. Atmos.* **104**, 31333–31349.
- Engelmann, R., Ansmann, A., Horn, S., Seifert, P., Althausen, D. and co-authors. 2011. Doppler lidar studies of heat island effects on vertical mixing of aerosols during SAMUM-2. *Tellus B* **63**, 448–458.
- Feingold, B., Girnita, A., Olesnevich, P., Zeevi, A., Quivers, E. S. and co-authors. 2006. Survival in allosensitized children after listing for heart transplantation. *J. Heart Lung Transpl.* **25**, S50–S50.
- Fernald, F. G., Herman, M. B. and Reagan, J. A. 1972. Determination of aerosol height distributions by lidar. *J. Appl. Meteorol.* **11**, 482–489.
- Fernald, F. G. 1984. Analysis of atmospheric lidar observations: some comments. *Appl. Opt.* **23**, 652–653.
- Fierz-Schmidhauser, R., Zieger, P., Gysel, M., Kammermann, L., DeCarlo, P. F. and co-authors. 2010. Measured and predicted aerosol light scattering enhancement factors at the high alpine site Jungfraujoch. *Atmos. Chem. Phys.* **10**, 2319–2333.
- Franke, K., Ansmann, A., Müller, D., Althausen, D., Wagner, A. and co-authors. 2001. One-year observations of particle lidar ratio over the tropical Indian Ocean with Raman lidar. *Geophys. Res. Lett.* **28**, 4559–4562.
- Freudenthaler, V., Esselborn, M., Wiegner, M., Heese, B., Tesche, M. and co-authors. 2009. Depolarization ratio profiling at several wavelengths in pure Saharan dust during SAMUM 2006. *Tellus B* **61**, 165–179.
- Ginoux, P. 2003. Effects of nonsphericity on mineral dust modeling. *J. Geophys. Res.-Atmos.* **108**, D2, 4052, 1–10.
- Granados-Muñoz, M. J., Navas-Guzmán, F., Bravo-Aranda, J. A., Guerrero-Rascado, J. L., Lyamani, H. and co-authors. 2012. Automatic determination of the planetary boundary layer height using lidar: one-year analysis over southeastern Spain. *J. Geophys. Res.-Atmos.* **117**, D18208, 1–10.
- Guerrero-Rascado, J. L., Olmo, F. J., Aviles-Rodriguez, I., Navas-Guzmán, F., Perez-Ramirez, D. and co-authors. 2009. Extreme Saharan dust event over the southern Iberian Peninsula in september 2007: active and passive remote sensing from surface and satellite. *Atmos. Chem. Phys.* **9**, 8453–8469.
- Heintzenberg, J., Wiedensohler, A., Tuch, T. M., Covert, D. S., Sheridan, P. and co-authors. 2006. Intercomparisons and aerosol calibrations of 12 commercial integrating nephelometers of three manufacturers. *J. Atmos. Ocean. Tech.* **23**, 902–914.
- Holben, B. N., Eck, T. F., Slutsker, I., Tanre, D., Buis, J. P. and co-authors. 1998. AERONET – a federated instrument network and data archive for aerosol characterization. *Remote Sens. Environ.* **66**, 1–16.
- Holzworth, G. C. 1964. Estimate of mean maximum mixing depths in the contiguous United States. *Mon. Weather Rev.* **92**, 235–242.
- Kim, J. Y., Magari, S. R., Herrick, R. F., Smith, T. J. and Christiani, D. C. 2004. Comparison of fine particle measurements from a direct-reading instrument and a gravimetric sampling method. *J. Occup. Environ. Hyg.* **1**, 707–715.
- Klett, J. D. 1981. Stable analytical inversion solution for processing lidar returns. *Appl. Optics.* **20**, 211–220.
- Klett, J. D. 1985. Lidar inversion with variable backscatter/extinction ratios. *Appl. Optics.* **24**, 1638–1643.
- Krueger, A. J. and Minzner, R. A. 1976. Mid-latitude ozone model for 1976 United-States standard atmosphere. *J. Geophys. Res.-Oc. Atm.* **81**, 4477–4481.
- Kwon, H. J., Cho, S. H., Chun, Y., Lagarde, F. and Pershagen, G. 2002. Effects of the Asian dust events on daily mortality in Seoul, Korea. *Environ. Res.* **90**, 1–5.
- Landulfo, E., Papayannis, A., Artaxo, P., Castanho, A. D. A., de Freitas, A. Z. and co-authors. 2003. Synergetic measurements of aerosols over Sao Paulo, Brazil using LIDAR, sunphotometer and satellite data during the dry season. *Atmos. Chem. Phys.* **3**, 1523–1539.
- Lyamani, H., Olmo, F. J. and Alados-Arboledas, L. 2008. Light scattering and absorption properties of aerosol particles in the urban environment of Granada, Spain. *Atmos. Environ.* **42**, 2630–2642.
- Lyamani, H., Olmo, F. J. and Alados-Arboledas, L. 2010. Physical and optical properties of aerosols over an urban location in Spain: seasonal and diurnal variability. *Atmos. Chem. Phys.* **10**, 239–254.
- Mishchenko, M. I., Travis, L. D., Kahn, R. A. and West, R. A. 1997. Modeling phase functions for dustlike tropospheric aerosols using a shape mixture of randomly oriented polydisperse spheroids. *J. Geophys. Res. Atmos.* **102**, 16831–16847.
- Müller, D., Franke, K., Ansmann, A., Althausen, D. and Wagner, F. 2003. Indo-Asian pollution during INDOEX: microphysical particle properties and single-scattering albedo inferred from multiwavelength lidar observations. *J. Geophys. Res.-Atmos.* **108**, D19, 1–15.
- Müller, D., Heinold, B., Tesche, M., Tegen, I., Althausen, D. and co-authors. 2009. EARLINET observations of the 14–22-May long-range dust transport event during SAMUM 2006: validation of results from dust transport modelling. *Tellus B* **61**, 325–339.
- Navas-Guzmán, F., Fernandez-Galvez, J., Granados-Munoz, M. J., Guerrero-Rascado, J. L., Bravo-Aranda, J. A. and co-authors. 2014. Tropospheric water vapour and relative humidity profiles from lidar and microwave radiometry. *Atmos. Meas. Tech.* **7**, 1201–1211.
- Navas-Guzmán, F., Bravo-Aranda, J. A., Guerrero-Rascado, J. L., Granados-Muñoz, M. J. and Alados-Arboledas, L. 2013. Statistical analysis of aerosol optical properties retrieved by Raman lidar over Southeastern Spain. *Tellus B* **65**, 21234. DOI: 10.3402/tellusb.v65i0.21234.

- Navas Guzmán, F., Guerrero Rascado, J. L. and Alados Arboledas, L. 2011. Retrieval of the lidar overlap function using Raman signals. *Óptica Pura y Aplicada* **44**, 71–75.
- Nemuc, A., Vasilescu, J., Talianu, C., Belegante, L. and Nicolae, D. 2013. Assessment of aerosol's mass concentrations from measured linear particle depolarization ratio (vertically resolved) and simulations. *Atmos. Meas. Tech.* **6**, 3243–3255.
- O'Neill, N. T., Dubovik, O. and Eck, T. F. 2001a. Modified Angström exponent for the characterization of submicrometer aerosols. *Appl. Opt.* **40**, 2368–2375.
- O'Neill, N. T., Eck, T. F., Holben, B. N., Smirnov, A., Dubovik, O. and co-authors. 2001b. Bimodal size distribution influences on the variation of Angstrom derivatives in spectral and optical depth space. *J. Geophys. Res. Atmos.* **106**, 9787–9806.
- Pappalardo, G., Amodeo, A., Pandolfi, M., Wandinger, U., Ansmann, A. and co-authors. 2004. Aerosol lidar intercomparison in the framework of the EARLINET project. 3. Raman lidar algorithm for aerosol extinction, backscatter, and lidar ratio. *Appl. Opt.* **43**, 5370–5385.
- Pappalardo, G., Amodeo, A., Apituley, A., Comeron, A., Freudenthaler, V. and co-authors. 2014. EARLINET: towards an advanced sustainable European aerosol lidar network. *Atmos. Meas. Tech.* **7** 2389–2409. DOI: 10.5194/amt-7-2389-2014.
- Perez, C., Nickovic, S., Baldasano, J. M., Sicard, M., Rocadenbosch, F. and co-authors. 2006. A long Saharan dust event over the western Mediterranean: lidar, sun photometer observations, and regional dust modeling. *J. Geophys. Res.-Atmos.* **111**, D15114, 1–16.
- Pérez, L., Tobias, A., Querol, X., Kunzli, N., Pey, J. and co-authors. 2008. Coarse particles from Saharan dust and daily mortality. *Epidemiology* **19**, 800–807.
- Petzold, A. and Schonlinner, M. 2004. Multi-angle absorption photometry – a new method for the measurement of aerosol light absorption and atmospheric black carbon. *J. Aerosol. Sci.* **35**, 421–441.
- Petzold, A., Schloesser, H., Sheridan, P. J., Arnott, W. P., Ogren, J. A. and co-authors. 2005. Evaluation of multiangle absorption photometry for measuring aerosol light absorption. *Aerosol Sci. Tech.* **39**, 40–51.
- Preissler, J., Wagner, F., Pereira, S. N. and Guerrero-Rascado, J. L. 2011. Multi-instrumental observation of an exceptionally strong Saharan dust outbreak over Portugal. *J. Geophys. Res.-Atmos.* **116**, D24204, 1–12.
- Preissler, J., Wagner, F., Guerrero-Rascado, J. L. and Silva, A. M. 2013. Two years of free-tropospheric aerosol layers observed over Portugal by lidar. *J. Geophys. Res. Atmos.* **118**, 3676–3686.
- Prospero, J. M. 1999. Long-term measurements of the transport of African mineral dust to the southeastern United States: implications for regional air quality. *J. Geophys. Res. Atmos.* **104**, 15917–15927.
- Rose, T., Crewell, S., Lohnert, U. and Simmer, C. 2005. A network suitable microwave radiometer for operational monitoring of the cloudy atmosphere. *Atmos. Res.* **75**, 183–200.
- Russel, P. B., Swissler, T. J. and McCormick, M. P. 1979. Methodology for error analysis and simulation of lidar aerosol measurements. *Appl. Opt.* **18**, 3783–3797. DOI: 10.1364/AO.18.003783.
- Schuster, G. L., Dubovik, O. and Holben, B. N. 2006. Angstrom exponent and bimodal aerosol size distributions. *J. Geophys. Res.-Atmos.* **111**, D07207, 1–14.
- Seinfeld, J. H. and Pandis, S. N. 1998. *Atmospheric Chemistry and Physics*. Wiley-Interscience.
- Shimizu, A., Sugimoto, N., Matsui, I., Arao, K., Uno, I. and co-authors. 2004. Continuous observations of Asian dust and other aerosols by polarization lidars in China and Japan during ACE-Asia. *J. Geophys. Res.-Atmos.* **109**, D19517, 1–14.
- Tesche, M., Ansmann, A., Müller, D., Althausen, D., Mattis, I. and co-authors. 2009. Vertical profiling of Saharan dust with Raman lidars and airborne HSRL in southern Morocco during SAMUM. *Tellus B* **61**, 144–164.
- Titos, G., Foyo-Moreno, I., Lyamani, H., Querol, X., Alastuey, A. and co-authors. 2012. Optical properties and chemical composition of aerosol particles at an urban location: an estimation of the aerosol mass scattering and absorption efficiencies. *J. Geophys. Res.-Atmos.* **117**, D04206.
- Titos, G., Lyamani, H., Pandolfi, M., Alastuey, A. and Alados-Arboledas, L. 2014a. Identification of fine (PM₁) and coarse (PM₁₀₋₁) sources of particulate matter in an urban environment. *Atmos. Environ.* **89**, 593–602.
- Titos, G., Lyamani, H., Cazorla, A., Sorribas, M., Foyo-Moreno, I. and co-authors. 2014b. Study of the relative humidity dependence of aerosol light-scattering in southern Spain. *Tellus B* **66**, 1–15. 24536. DOI: 10.3402/tellusb.v66.24536.
- Wandinger, U. and Ansmann, A. 2002. Experimental determination of the lidar overlap profile with Raman lidar. *Appl. Optics.* **41**, 511–514.
- Wang, Z., Cao, X., Zhang, L., Notholt, J., Zhou, B. and co-authors. 2012. Lidar measurement of planetary boundary layer height and comparison with microwave profiling radiometer observation. *Atmos. Meas. Tech.* **5**, 1965–1972.